Rock Climbing-Inspired Electrohydrodynamic Cryoprinting of Micropatterned Porous Fiber Scaffolds with Improved MSC Therapy for Wound Healing

Rock Climbing-Inspired Electrohydrodynamic Cryoprinting of Micropatterned Porous Fiber Scaffolds with Improved MSC Therapy for Wound Healing

Cite this Accepted Manuscript (AM) as Accepted Manuscript (AM) version ofJinjian Huang, Jie Wu, Jiahang Wang, Mengjia Xu, Jiao Jiao, Yuhao Qiang, Feng Zhang, Zongan Li, Rock Climbing-Inspired Electrohydrodynamic Cryoprinting of Micropatterned Porous Fiber Scaffolds with Improved MSC Therapy for Wound Healing, Advanced Fiber Materials https://doi.org/10.1007/s42765-022-00224-w

Rock climbing-inspired electrohydrodynamic cryoprinting of micropatterned porous fiber scaffolds with improved MSC therapy for wound healing

Jinjian Huang[1#], Jie Wu[1#], Jiahang Wang[2#], Mengjia Xu[2], Jiao Jiao[1], Yuhao Qiang[3*], Feng Zhang[*], Zongan Li[2*]

[1] Research Institute of General Surgery, Jinling Hospital, School of Medicine, Southeast University, Nanjing, 210009, China;

[2] Jiangsu Key Laboratory of 3D Printing Equipment and Manufacturing, NARI School of Electrical and Automation Engineering, Nanjing Normal University, Nanjing, 210042, China;

[3] Department of Materials Science and Engineering, Massachusetts Institute of Technology, Cambridge 02139, USA.

*** Correspondence to:**

Yuhao Qiang, e-mail: Yuhqiang@mit.edu;

Feng Zhang, e-mail: fengzhan@njnu.edu.cn;

Zongan Li, e-mail: Zongan_li@njnu.edu.cn.

[#] These authors contributed equally to this work.

Abstract

Impaired wound healing poses great health risks to patients. Recently, mesenchymal stem cell (MSC) therapy has shown potential to improve the healing process, but approaches to employ MSCs in the treatment of wounds remain elusive. In this study, we reported a novel electrohydrodynamic (EHD) cyroprinting method to fabricate micropatterned fiber scaffolds with polycaprolactone (PCL) dissolved in glacial acetic acid (GAC). Cyroprinting ensured the formation of a porous structure of PCL fibers by preventing the evaporation of GAC, thus increasing the surface roughness parameter Ra from 11 to 130 nm. Similar to how rough rocks facilitate easy climbing, the rough surface of fibers was able to increase the adhesion of adipose-derived MSCs (AMSCs) by providing more binding sites; therefore, the cell paracrine action of secreting growth factors and chemokines was enhanced, promoting fibroblast migration and vascular endothelial cell tube formation. In rat models with one-centimeter wound defects, enhanced MSC therapy based on porous PCL fiber scaffolds improved wound healing by augmenting scarless collagen deposition and angiogenesis and reducing proinflammatory reactions. Altogether, this study offers a new and feasible strategy to modulate the surface topography of polymeric scaffolds to strengthen MSC therapy for wound healing.

Keywords: electrohydrodynamic cryoprinting; porous fiber scaffolds; mesenchymal stem cell; wound healing

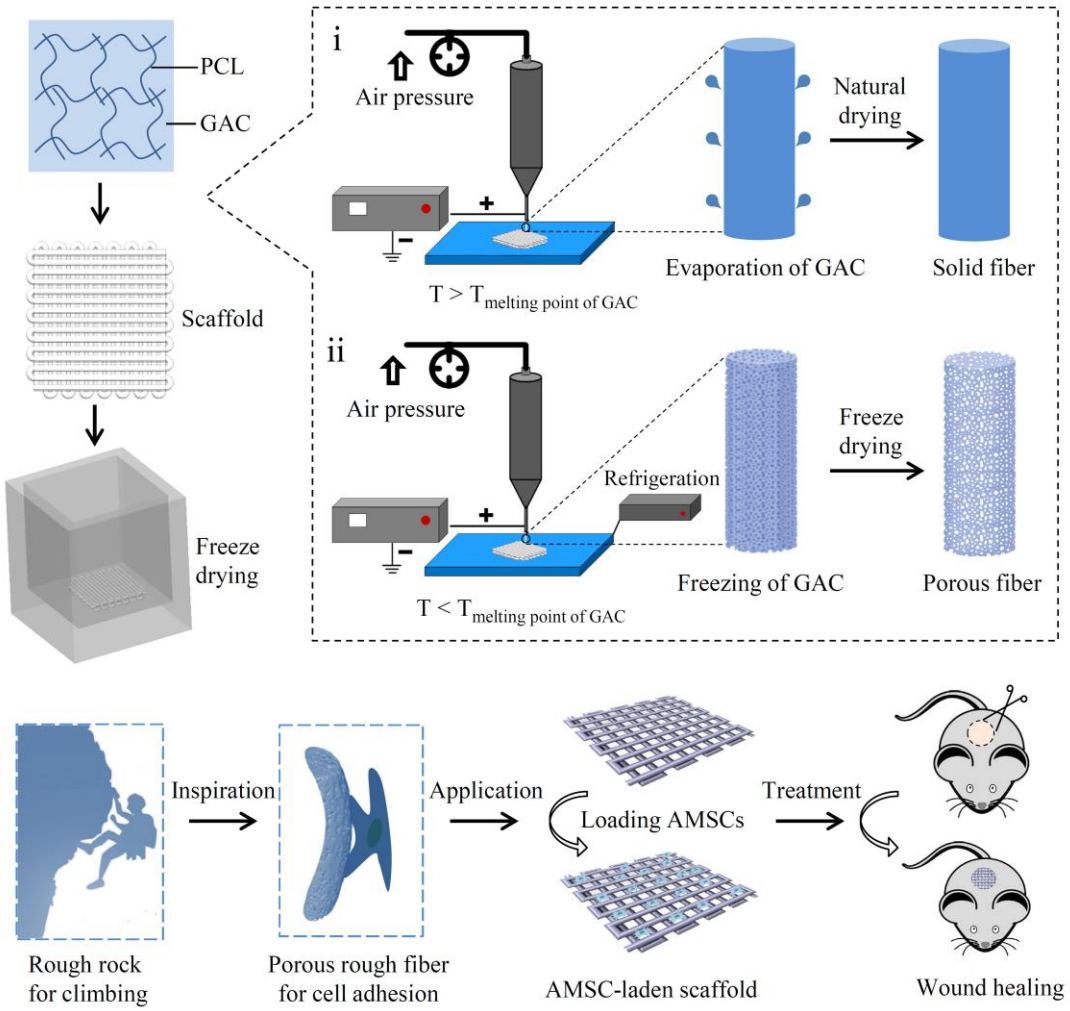

Graphic abstract

1. Introduction

Impaired skin wound healing is an intractable issue in clinical work and is vulnerable to various conditions such as microbial infections, large skin defects, diabetes mellitus, and malnutrition [1,2]. Moreover, patients complicated with non-healing wounds are more likely to suffer from pain, scarring, delayed discharge, and even severe complications such as amputation and life-threatening bacteremia [3,4]. It was reported that the costs for wound repair reached $20 billion and €4–6 billion annually in the USA and EU, respectively [5]. To address this problem, many types of new biomaterials and tissue engineering products have been developed, including microfibers, foam, sponges, and hydrogels, for use individually or in combination with therapeutic drugs [6-9]. However, these products still lack extensive bioactivities involved in all-phase wound healing from inflammation, and proliferation to tissue remodeling.

In recent years, mesenchymal stem cell (MSC) therapy has been developed and exhibits therapeutic effectiveness during all stages of wound healing [10-13]. Mechanistically, MSCs can directly differentiate into interstitial cells (e.g., fibroblasts, keratinocytes, epithelial cells, and endothelial cells) and secrete growth factors (e.g., TGF-β and VEGF), immunomodulatory factors (e.g., IL-6 and IL-10), extracellular matrix (ECM) molecules (e.g., Fibronectin-1 and collagen I-IV), ECM proteases (e.g., MMP-2 and MMP-3) and miRNA-carried exosomes (e.g., miR-21, -23a, -125b, and -145) to provide seeding cells and regulate molecular signaling pathways of tissue regeneration [14,15]. More excitingly, such MSC therapy has been clinically translated as a safe and effective method to treat non-healing wounds caused by diabetic foot ulcers [16]. Despite these advancements, the technologies used to recruit sufficient MSCs to the lesion site, such as bioprinted hydrogels and polymeric scaffolds, remain immature due to inevitable cell damage, inadequate cell nutrient supply, and limited cell-carrying capacity. For example, MSCs within the hydrogel would be injured due to mechanical shearing from extrusion-based bioprinting or oxidative stress caused by light-curing bioprinting [17]. Compared with bioprinting, MSC-seeded polymeric scaffolds do not damage cells, but the processes of seeding

MSCs and adhering them onto the scaffolds are time-consuming and inefficient [18], which hinders the popularization of MSC therapy for wound healing.

Given increased insight into cell adhesion to polymeric scaffolds, cell behaviors were identified that mimicked humanized patterns. Specifically, Xie *et al.* [19] reported that cells tended to grab scaffolds consisting of finer fibers by elongating cell bodies in a manner to human hands to grab fine objects more easily. Inspired by this notion, we aimed to engineer a rough surface for scaffold fibers to enhance the MSC adhesion and improve therapeutic effects following the principle of "rough rocks for easier climbing". To achieve this goal, we fabricated porous polycaprolactone (PCL) fiber scaffolds by electrohydrodynamic (EHD) cryoprinting.

EHD printing, which draws fluid out of the nozzle by electric field force, can be used to fabricate highly-ordered and shape-customized fine polymeric scaffolds [20,21]. PCL is a cationic polymer with good flexibility, biocompatibility, and temperature-induced phase change ability; therefore, it has been widely used in 3D printed tissue engineering scaffolds [22,23]. Cryoprinting is an emerging hotspot in 3D printing because it can maintain structural fidelity and restore the bioactivities of printed living tissues [24-26]. In this study, PCL was dissolved in glacial acetic acid (GAC) and printed with EHD. Cryoprinting was achieved with the help of a cryogenic substrate to eliminate GAC evaporation. The frozen GAC was sublimated with freeze drying, forming a multiscale porous structure of PCL fibers. Through this process, the fabricated PCL scaffolds featured a pore-induced rough surface, thus promoting cell adhesion competence and enhancing MSC therapy for wound healing.

2. Materials and methods

2.1 Materials

PCL (MW~80,000) was purchased from Jinan Daigang Bioengineering Co., Ltd, China. GAC (purity>99.7%) was purchased from Shanghai Aladdin Technology Co., Ltd, China. A metal conductive nozzle (25G; inner diameter, 260 μm; outer diameter 510 μm, length 25 mm) was provided by Aroh Alona Company, China.

2.2 Preparation of PCL scaffolds

PCL particles were dissolved in GAC at 60 ℃ and stirred continuously at 200 rpm for 6 hours to prepare a 40 wt% homogeneous PCL/GAC solution. Then, the bubbles were expelled using a vacuum drying oven (DZF-6050, Shanghai Jinghong Experimental Equipment Co., Ltd, China). The degased solution was fed into a 5 ml plastic dispensing syringe for printing.

The prepared PCL/GAC solution was jetted with the EHD cryoprinting system as shown in **Fig. S1a** and **Video S1**. This system included a three axis moving system, a signal generator, a high voltage amplifier (AS-3B1-A, Matsusada Precision, Japan), a pneumatic control system, and a cryogenic substrate. The substrate was refrigerated to -20 ℃ (well below the melting point of GAC 16.6 ℃) using a thermoelectric cooler, and a syringe containing the PCL/GAC solution was connected to the pneumatic control system assembled with an air pump and a micro pressure regulating valve. Finally, the positive pole of the high voltage amplifier was connected to the metal nozzle, and the negative pole was attached to the substrate. After the predesigned shape was printed, it was placed into a freezer dryer (LGJ-20F, SongYuan, China) to sublimate GAC for 24 hours at -43 ℃, which resulted the porous structure of PCL fibers. For the fibers with solid struts, the PCL/GAC solution was jetted onto a substrate at 25 ℃ (above the melting point of GAC 16.6 ℃), which facilitated the rapid evaporation of GAC. No pores were formed in the structures.

2.3 Micromorphology of PCL scaffolds

The PCL scaffolds were observed with a scanning electron microscope (SEM,

JSM-5610LV, JEOL, Japan). Specifically, after coating with a thin layer of gold, the images of PCL scaffolds with or without cryoprinting were recorded using SEM.

2.4 Regulation of PCL scaffolds

The simulation of the shape changes of the cone jet under different voltages and inlet pressures of EHD cryoprinting was conducted based on the finite element method using COMSOL Multiphysics 5.6. The Navier–Stokes equation was used to describe the momentum conservation for incompressible viscous fluids, as noted in Eq. (1):

$$\rho\frac{\partial u}{\partial t}+\nabla\cdot(\rho uu)=\rho g-\nabla P+\mu\nabla^2 u+F_{st}+f \quad \text{Eq. (1)}$$

where ρ is the fluid density, u is the fluid velocity, t is the time, P is the pressure, μ is the fluid viscosity, F_{st} is the surface tension, and f is the electric field force under the electrostatic field. The model and parameters for the simulation are listed in **Table 1**.

Table 1. The model and parameters for simulation of conical jet of EHD cryoprinting

Model	Parameter	Description	Value	Notes
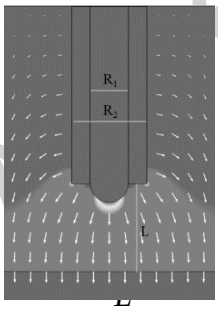	F_{st}	surface tension	28 mN/m	[27,28]
	Rp	relative permittivity of PCL/GAC solution	6.2	[29]
	Rp_{air}	relative permittivity of air	1	-
	μ	dynamic viscosity of PCL/GAC solution	50 mPa·s	**Fig. S1b**
		dynamic viscosity of air	17.9×10^{-6} Pa·s	-
		density of PCL/GAC solution	1.056 g/cm^3	-
		density of air	1.29×10^{-3} g/cm^3	-
		inner diameter of nozzle	0.26 mm	-
		outer diameter of nozzle	0.51 mm	-
		distance between nozzle and substrate	0.6 mm	-

To verify the accuracy of the simulation results, we compared the actual fiber size of PCL scaffolds by adjusting the voltages (1,000-4,000 V) and inlet pressures (8-15

kPa) of EHD cryoprinting. In addition, the impact of the printing speed (5-35 mm/s) on the fiber size was also investigated.

2.5 Transparency of PCL scaffolds

For a visual display of the transparency, the scaffolds with solid fibers or with porous fibers were covered on the surface of the Southeast University logo. To quantitatively analyze the transmittance, we scanned the absorbance (A) of three-layer scaffolds using a UV–vis spectrophotometer (PerkinElmer, USA) at wavelengths from 300 to 700 nm with a scanning speed of 5 nm/s. The transmittance (T) was calculated using Eq. (2).

$$T = 1 / 10^{A} \quad \text{Eq. (2)}$$

2.6 Mechanical strength of PCL scaffolds

The stretching capabilities of PCL scaffolds with different fiber microstructures were measured using a universal material testing machine (MTS, model: CMT2103, USA) based on our previous methodology [30]. Specifically, the three-layer PCL scaffolds with a length of 20 mm (L_0) and a width of 10 mm were clamped by two parallel metal clips, and stretched to a new length (L_n) with a recorded force (F) at a rate of 20 mm/min until the scaffolds were broken. During this process, a tensile stress (τ)–strain (ε) curve was obtained. The Young's modulus was calculated based on longitudinal stress divided by the strain using Eq. (3).

$$\text{Young's modulus} = (FL_0) / A(L_n - L_0) \quad \text{Eq. (3)}$$

Area (A) was 2D data, and could be expressed as width (W = 10 mm) × layers (L_a = 3); therefore, Young's modulus could also be described as Eq. (4) and used for comparison when L_a = 3 had been predetermined.

$$\text{Young's modulus} = (FL_0) / WL_a(L_n - L_0) \quad \text{Eq. (4)}$$

The fracture energy (U) of the scaffolds was calculated using Eq. (5) based on the integral of the area under the tensile stress (τ)–strain (ε) curve.

$$U = \int \tau \mathrm{d}\varepsilon \quad \text{Eq. (5)}$$

The tensile stress (τ) was expressed as F/A; therefore, the fracture energy could also

be described as Eq. (6), and used for comparison when L_a = 3 had been predetermined.

$$U = 1/WL_a\int Fd\varepsilon \quad \text{Eq. (6)}$$

2.7 Surface topography of PCL scaffolds

The PCL scaffold was fixed on a glass slide, and a single fiber was randomly chosen and photographed using a Bruker Dimension Icon AFM instrument in a scanning range of 10 μm × 10 μm. The average roughness parameter Ra was automatically reported by the NanoScope Analysis software.

2.8 Adhesion of adipose-derived MSCs (AMSCs) to PCL scaffolds

AMSCs were harvested from inguinal adipose tissues of 6-week-old Sprague–Dawley (SD) rats (Huachuang Sino Co., Ltd, Jiangsu, China) according a previously reported approach with slight modifications [31]. Briefly, after the rats were sacrificed, the inguinal adipose tissues were surgically separated, washed and cut into small pieces. The pieces were digested with 1 mg/mL collagenase II (BS164, biosharp) diluted with DMEM/F-12 culture medium (KeyGen BioTECH Co., Ltd, China) at 37 °C for 30 min. Subsequently, the medium was filtered with a 70-μm cell strainer, and the digestion process was terminated by adding an equal amount of culture media. The resultant AMSC-mixed solution was centrifuged at 1000 rpm/min for 5 min, and the supernatant was discarded. The obtained AMSCs were then seeded onto a 10-cm cell culture dish, and cultured with complete DMEM/F-12 medium in a cell incubator (37 °C, 5% CO_2). AMSCs at passages 2–4 were used for further studies. This protocol was approved by the Animal Investigation Ethics Committee of Jinling Hospital (NO. 2020JLHSKJDWLS-123).

The adhesion of AMSCs (5×10^4 cells) to PCL scaffolds (10 mm × 10 mm) was conducted in a 24-well ultralow adsorption plate (AMA Co., Ltd, China), which allowed the cells to adhere to the scaffolds instead of the bottom of the plate. Then, the cells were cultured with complete DMEM/F-12 medium in the incubator for use in the following experiments.

2.9 Live/dead staining

Eight hours after seeding AMSCs, the scaffolds (10 mm × 10 mm) were removed from the culture plate and rinsed with phosphate buffer saline (PBS). Then, the AMSC-laden scaffolds were stained with 2 μM calcein AM and 8 μM PI (KeyGen BioTECH Co., Ltd, China) for 30 min followed by imaging with a confocal microscope (FV3000, Olympus, Japan) using the *Z*-stack mode.

2.10 Cell count kit-8 (CCK-8) assay

Following AMSC adhesion to scaffolds for different durations (1 d and 2 d), the scaffolds (10 mm × 10 mm) were transferred to a new 24-well cell plate and rinsed with PBS. CCK-8 reagent (Vazyme Biotech Co., Ltd, China) was added to the plate for an additional 30 min of culture. Then, the absorbance of plate was detected with a microplate reader (BioTek, USA) at 450 nm. The scaffolds with solid or porous fibers were used in triplicate to compare the number of attached AMSCs.

2.11 Cytoskeleton staining

AMSCs were added to a 24-well ultralow adsorption plate with PCL scaffolds. Eight hours later, the scaffolds were washed with PBS and fixed in 4% methanol-free paraformaldehyde solution. Triton X-100 (0.1%) in PBS and 1% bovine serum albumin (BSA) solution were used to permeabilize cells and reduce nonspecific background staining, respectively. Afterwards, we diluted 5 μL methanolic stock solution containing 6.6 μM Alexa Fluor Plus 555 phalloidin into 200 μL PBS for each scaffold to be stained at room temperature for 20 min, followed by repeated PBS washes. Nuclei were stained with DAPI (KeyGen BioTECH Co., Ltd, China) for 15 min. Finally, the AMSCs were imaged using the *Z*-stack mode of the confocal microscope. The cell spreading area was determined using ImageJ (NIH, USA) by randomly calculating fifteen AMSCs.

2.12 Enzyme-linked immunosorbent assay (ELISA)

After eight hours of AMSC adhesion to the PCL scaffolds, the scaffolds were transferred to a new plate for an additional 3 days of culture. The cell supernatant was collected, and the cytokines were detected with commercial ELISA kits including the vascular endothelial cell growth factor a (VEGF-A) kit (E-EL-R2603c, Elabscience, China), monocyte chemotactic protein 1 (MCP-1) kit (E-EL-R0633c, Elabscience, China), and transforming growth factor beta 1 (TGF-β1) kit (E-EL-0162c, Elabscience, China) according to the manufacturer's instructions.

2.13 Wound healing assay

Green fluorescent protein (GFP)-expressing L929 cells ($L929^{GFP+}$) were constructed with *GFP* gene-inserted lentivirus (SyngenTech, China). $L929^{GFP+}$ cells (600 μL, 5×10^4 /mL) were seeded in the lower chamber of a 24-well transwell plate (Corning, USA), and cultured overnight in DMEM with 10% fetal bovine serum (FBS). On the next day, a scratch was created using a 20 μm pipette, and the detached cells were removed with PBS washes. Then, the attached cells were cultured in DMEM with 2% (v/v) FBS. Simultaneously, the scaffolds with attached AMSCs were placed into the upper chambers of the transwell plate, and cultured in 200 μL of complete DMEM/F-12 medium overnight. At pre-set time points (0 h, 24 h, 48 h), the healing process of the defective wound was recorded with a fluorescence microscope (CKX53, Olympus, Japan), and analyzed using ImageJ. Each treatment was performed in triplicate.

2.14 Tube formation assay

HUVECs (500 μL, 5×10^4 /mL, P2-P4, ScienCell, USA) were added to the Matrigel (356231, BD, USA)-coated lower chamber of a 24-well transwell plate and cultured in complete ECM medium (ScienCell, USA). Simultaneously, AMSC-laden PCL scaffolds were placed into the upper chambers, and cultured in 200 μL of complete DMEM/F-12 medium. Six hours later, tube formation was recorded with a microscope (CKX53, Olympus, Japan), and analyzed using ImageJ based on three different visual fields (VSs).

2.15 Bacterial proliferation and biofilm formation

To test the effects of materials on bacterial growth and biofilm formation, *P. aeruginosa* (ATCC 27853) was used as a model bacterium. Specifically, *P. aeruginosa* was incubated in 3 mL Luria-Bertani (LB) broth (Solarbio, China) at a concentration of 1×10^8 colony forming units (CFU)/mL and co-cultured with 10 mm × 20 mm materials (i.e., gauze, solid fiber scaffold, or porous fiber scaffold). LB broth containing only *P. aeruginosa* was defined as a blank group. The prepared LB broth was shaken at 37 °C for 24 hours. At each pre-set time point, 100 μL of LB broth in different groups was harvested to measure the optical density (OD) value with a microplate reader at the absorbance of 600 nm for to generate bacterial growth curves, which were used to determine the antibacterial abilities of the materials [32].

Moreover, biofilm formation reflects the bacterial attachment capabilities toward materials, which can be measured with the crystal violet biofilm staining assay [33,34]. In details, the materials were removed from the LB broth after 24 hours of co-culture, and cut into 5 mm × 5 mm pieces. Subsequently, the material samples were stained with commercially prepared crystal violet (Beyotime, China) for 10 min, followed by three PBS washes. The stained materials were air-dried overnight, and then immersed in 200μL of 30 v/v% acetic acid (Aladdin, China) to dissolve the remaining crystal violet. The OD value of the dissolved solution was detected with a microplate reader at an absorbance of 570 nm. Each material was experimentally analyzed in triplicate.

2.16 Animal experiments

Thirty-two male SD rats weighing approximately 220 g were housed in individual cages with free access to sterile water and standard chow, controlled temperature, and natural light-dark cycles. The wound models were created by the removal of a 1-cm diameter circular sample of full-thickness skin from the backs of rats. Afterwards, the rats were randomly divided into four groups evenly with each group treated with gauze, simple porous fiber scaffold, solid fiber scaffold + AMSCs [$(2.19 \pm 0.13) \times 10^4$

cells], or porous fiber scaffold + AMSCs [(3.03 ± 0.18) × 10^4 cells]. Then, the wounds in each group were fixed with surgical tape to prevent the gauze or the scaffolds from falling off [35,36]. The gauze or the scaffolds were changed every day until the 4th day when scabs were formed. This animal protocol was approved by the Animal Care and Use Committee of Jinling Hospital (NO. 2020JLHSKJDWLS-123).

Four days later, the blood supply of regenerated skin was evaluated with noninvasive laser speckle contrast analysis (LASCA) using moorFLPI-2 (Moor Instruments, UK). The blood flow could be reflexed by mean flux. Moreover, on the 7th day postoperatively, half of the rats in each group were sacrificed and the granulation tissues were harvested. The tissues were then fixed with 10% neutral formaldehyde and analyzed with HE staining, Masson's trichrome staining, Sirius red staining, immunofluorescence (IF) staining of vascular structures with CD 31 antibody (MA5-16951, Invitrogen, USA) and α-SMA antibody (GB111364, Servicebio, China), and IF staining of proinflammatory cytokines with IL-6 antibody (GB11117, Servicebio, China) according to the regular procedures [37]. The semiquantitative analysis was performed on eight random VSs with two VSs for each sample. The other half of the rats survived for continuous observation of the wound closure process.

2.17 Data analysis

Data were analyzed using GraphPad Prism 9 software by Student's t test (unpaired and two-tailed) or one-way ANOVA (analysis of variance). Multiple comparisons were performed if needed. The values were considered significantly different when the p value was less than 0.05.

13

3. Results and discussion

3.1 Structure and properties of PCL scaffolds with EHD cyroprinting

In principle, EHD cryoprinting was able to inhibit the evaporation of GAC in PCL fibers compared with traditional EHD printing; therefore, a specific porous microstructure was created within the fibers (**Fig. 1a**). Such a porous microstructure served as an anchor point to increase AMSC adhesion in a manner similar to rough rocks facilitating rock climbing. This feature could be expected to enhance MSC therapy for wound healing (**Fig. 1b**).

The appearance of PCL scaffolds fabricated by EHD cryoprinting featured a reduction in transparency (**Fig. 2a**). Quantitatively, the transmittance of the PCL scaffold with cryoprinting was approximately five-fold less than that of scaffolds without freezing treatment at an ultraviolet (UV) light wavelength of 360 nm and a visible light wavelength of 500 nm (**Fig. 2b**). This finding implied that the cryoprinted PCL scaffold could prevent light-induced injury to seeded cells when applied to the body surface [38,39]. The micromorphology of the cryoprinted fibers appeared to be porous under SEM observation, whereas the non-cryoprinted fibers were solid (**Fig. 2c**). The microstructure difference was responsible for the varied transmittance as the pores in the fibers could lead to light scattering, thus reducing light transmission (**Fig. 2d**).

EHD cryoprinting also affected the mechanical strength as measured using a universal material testing machine (**Fig. 2e**). As shown in **Fig. 2f**, the tensile stress–strain curve indicates that the tensile strength and elongation at break were significantly decreased for the scaffolds consisting of porous fibers. More accurately, the tensile strength was approximately 50 N/m/layer for solid fiber scaffolds and 5 N/m/layer for porous fiber scaffolds. The elongation at break was reduced from ~13% to ~3% when cryoprinting was applied. The Young's modulus and fracture energy only remained 13% and 2.4%, respectively (**Fig. S2**). These data suggest that the porous structure makes the scaffold fragile, and more caution should be taken when EHD cryoprinting is utilized.

3.2 Geometric control of PCL scaffolds by EHD cyroprinting

The PCL/GAC liquid at the Taylor cone tip is subjected to an electric field force F_{es}, gravity F_g, surface tension F_{st}, and viscous force F_u. The liquid at the lateral sides of the Taylor cone is subjected to the normal phase electric field force $F_{es,N}$, tangential electric field force $F_{es,T}$, surface tension F_{st} ,and gas phase pressure F_2. In addition, the liquid pressure F_1 in the nozzle was also applied on the liquid cone (**Fig. 3a**). As the voltage increased, the electric field force exceeded the surface tension such that the PCL/GAC liquid was expelled from the Taylor cone. In this situation, the force analysis at the tip of the Taylor cone followed the Eq. (7), and the force in the N direction at the lateral part of Taylor cone was balanced as described in Eq. (8), which allowed the conical jet to be stable.

$$F_g + F_{es} + F_1 > F_u + F_{st} + F_2 \quad \text{Eq. (7)}$$

$$F_1 + F_{es,N} = F_{st} + F_2 \quad \text{Eq. (8)}$$

Then, we simulated how the voltage and liquid pressure impacted the formation of scaffold fibers using COMSOL Multiphysics 5.6 in a coupled flow and electric field. It was revealed that the increase in voltage and air pressure on the PCL solution increased the width of the conical jet (**Fig. 3b, c**). Moreover, when the voltage was too high (> 4,000 V), it caused the split conical jet, which would affect the printing accuracy. Experimental studies showed a completely consistent trend with the simulated relationships between the voltage/air pressure and the jet width (**Fig. 3d, e** and **Fig. S3, S4**). The printing speed was also capable of negatively regulating the width of the printed fibers (**Fig. 3f** and **Fig. S5**).

In addition, the pattern creatability of scaffolds determined the applicable fields of tissue engineering products [40,41]. Thus, we fabricated various PCL scaffolds with assorted designed shapes, such as circles, pentagrams, loving hearts, and butterflies, using EHD cryoprinting (**Fig. 4a-c**). Specifically regarding wound treatment, such scaffolds could adapt to wound profiles with different shapes. Furthermore, internal fiber arrangement influences the biological interactions between scaffolds and seeded cells [42]; therefore, we further confirmed that the EHD cryoprinted PCL scaffolds could be fabricated with fibers crossed at different angles

(e.g., 30°, 45°, 60°, and 90°) (**Fig. 4d-f**). Overall, these data reflected an equivalently high geometry control capability regardless of the use of cryoprinting.

3.3 Improved cell therapy *in vitro* with the multiscale porous PCL scaffold

AMSCs were co-cultured with the solid or porous fiber PCL scaffolds in a 24-well ultralow adsorption plate. Eight hours later, we conducted live/dead staining on the cell-laden scaffolds. The results turned out that AMSCs more easily attached to porous fiber scaffolds (**Fig. 5a**). Quantitative analysis by CCK-8 assay also indicated that the counts of AMSCs adhering to porous fiber scaffolds exceeded those in solid fiber scaffolds on Day 1 and Day 2 (**Fig. 5b**). To explore the potential reasons, the cytoskeleton (F-actin) of AMSCs was stained with phalloidin because cell adherence and crawling were mainly mediated by the intracellular forces of the cytoskeleton and their transmission to an extracellular substrate through specific adhesion molecules [43]. It was revealed that the cell protrusions were more prominent (**Fig. 5c**), and the cell spreading area was significantly increased in porous fiber scaffolds compared to those of the cells attached to solid fiber scaffolds (**Fig. 5d**) after eight hours of co-culture. Given that the surface roughness of porous fibers was enlarged ~13-fold compared to that of solid fibers (**Fig. 5e, f**), such scaffolds could provide more binding sites for the adhesion molecules of AMSCs (**Fig. 5g**).

Based on a cell-interactive transwell model *in vitro* (**Fig. 6a**), the increase in AMSC adhesion to scaffolds improved cell therapy due to the enhanced secretion of cytokines such as VEGF, MCP-1, and TGF-β1 (**Fig. 6b**), which were involved in diverse biological functions including cell chemotaxis, angiogenesis, and tissue regeneration [44,45]. Specific to fibroblasts and HUVECs, more attached AMSCs in porous fiber scaffolds could lead to faster fibroblast migration (**Fig. 6c, d**) and better vascular endothelial cell tube formation (**Fig. 6e, f**). Thus far, we have confirmed that topography-modulated PCL scaffolds could improve the AMSC seeding efficiency to achieve enhanced cell functions.

3.4 Wound healing behavior of scaffolds with enhanced AMSC adhesion efficacy

We further investigated the effects of AMSC-laden porous fiber scaffolds on wound healing by controlled comparison of gauze, simple porous fiber scaffolds, and AMSC-laden solid fiber scaffolds (**Fig. 7a**). The healing process recorded in **Fig. 7b** shows that AMSC-laden porous fiber scaffolds contributed to a more rapid wound closure compared with the other treatments (**Fig. 7c**).

Moreover, four days postoperatively, the signals of blood flow in the wounds treated with porous fiber + AMSCs were the strongest among all the interventions evaluated by LASCA (**Fig. 7d, e**). On the 7^{th} day, the regenerated tissues analyzed with HE staining indicated that treatment with porous fiber + AMSCs caused thicker granulation tissues (**Fig. 7f, g**). These data suggested that the use of porous fiber + AMSCs was an optimal cell therapy because it promoted angiogenesis and provided a satisfying granulation basis for tissue epithelialization and dermis replacement [46].

Based on a detailed histological analysis of granulation tissues, we further verified that collagen deposition was more pronounced in wounds treated with AMSC-laden porous fiber scaffolds (**Fig. 8a, b**). However, such therapy would not increase the scarring risks [47] given that the collagen I/III ratio measured with Sirius red staining was increased and close to the value (~ 27) detected in normal rat skin (**Fig. 8c, d**). In addition, the density of blood vessels was increased (**Fig. 8e, f)**, and proinflammatory cytokines (e.g., IL-6) were decreased in the wounds treated with porous fiber + AMSCs (**Fig. 8g, h**). These outcomes validated the improvement of angiogenic and immunomodulatory functions achieved by the AMSC-loaded EHD cryoprinted PCL scaffolds.

Of note, despite the effectiveness of these cell-laden porous fiber scaffolds on wound healing, care should be taken when the wound becomes infected because the biomaterials lack antibacterial abilities (**Fig. S6a, b**). Of particular concern is that the roughness of porous fibers would increase the bacterial attachment and biofilm formation compared with solid fibers; however, the situation was much better than the use of traditional gauze (**Fig. S6c, d**). Therefore, at the present stage, cryoprinted porous fiber scaffolds are recommended for the treatment of clean wounds alone or in combination with other antibacterial agents for the treatment of infected wounds.

Altogether, AMSC-laden cryoprinted PCL scaffolds were verified to accelerate wound healing given their increased cell-carrying competence, through which AMSCs could perform most biological functions, including direct cell replacement, growth factor secretion, exosome delivery, and ECM remodeling, consequently regulating molecular signaling pathways of tissue regeneration [48]. When wounds are infected, the use of such scaffolds needs to be reconsidered.

18

4. Conclusion

Polymeric scaffolds have been widely used in tissue engineering and regenerative medicine. To date, EHD cryoprinting was proposed in this study to fabricate topography-modulatory PCL scaffolds by inducing porous structures within fibers. The fabricated fibers could provide more binding sites for AMSC adhesion, thus offering a highly efficient cell-carrying platform and improving the therapeutic effects of stem cell therapy for various treatments, such as wound healing. Moreover, as a 3D printed product, this porous fiber scaffold could be generated in various shapes and with different internal fiber arrangements as desired; therefore, the scaffold could be adapted to treat a majority of wounds found in the clinic. In addition, AMSC-loaded polymeric scaffolds that were used to cover wounds were easily damaged by UV from the outer environment due to cellular oxidative stress; therefore, the decreased transmittance of porous PCL scaffolds due to cryoprinting was able to prevent such light-induced injury to seeded stem cells and prolong the effect duration. In conclusion, this study offers exquisite and easily processed porous fiber scaffolds through EHD cryoprinting to construct a high-loading stem cell platform and enhance wound healing based on MSC therapy.

Acknowledgment

We thank the Postdoctoral Fund of Jinling Hospital (49154), the Postdoctoral Innovation Talents Support Program (BX20220393), the Nanjing Medical Science and Technology Development Project (ZKX17017), and the National Natural Science Foundation of China (32171402) for financial support.

Author contributions

Zongan Li, Yuhao Qiang, Feng Zhang, and Jinjian Huang: conceptualization; Zongan Li, and Jinjian Huang: funding acquisition; Jinjian Huang, Jie Wu, Mengjia Xu, Jiahang Wang, Jiao Jiao, Feng Zhang, and Zongan Li: investigation; Jinjian Huang, and Zongan Li: methodology and software; Zongan Li, and Yuhao Qiang: supervision and validation; Jinjian Huang: writing the original draft; Jiahang Wang, Jie Wu, and Feng Zhang: review & editing & revision.

Competing interests

The authors declare that they do not have any competing interests.

Data and materials availability

All of the data needed to evaluate the conclusions in the paper are presented in the paper and/or the Supplementary Materials.

References:

1. Maschalidi S, Mehrotra P, Keceli BN, De Cleene H, Lecomte K, Van der Cruyssen R, Janssen P, Pinney J, van Loo G, Elewaut D, Massie A, Hoste E, Ravichandran KS: Targeting SLC7A11 improves efferocytosis by dendritic cells and wound healing in diabetes. NATURE 2022;606:776-784.
2. Huang J, Ren J, Chen G, Li Z, Liu Y, Wang G, Wu X: Tunable sequential drug delivery system based on chitosan/hyaluronic acid hydrogels and PLGA microspheres for management of non-healing infected wounds. Mater Sci Eng C Mater Biol Appl 2018;89:213-222.
3. Wang Y, Beekman J, Hew J, Jackson S, Issler-Fisher AC, Parungao R, Lajevardi SS, Li Z, Maitz P: Burn injury: Challenges and advances in burn wound healing, infection, pain and scarring. Adv Drug Deliv Rev 2018;123:3-17.
4. Leithead C, Novak Z, Spangler E, Passman MA, Witcher A, Patterson MA, Beck AW, Pearce BJ: Importance of postprocedural Wound, Ischemia, and foot Infection (WIfI) restaging in predicting limb salvage. J VASC SURG 2018;67:498-505.
5. Pang C, Ibrahim A, Bulstrode NW, Ferretti P: An overview of the therapeutic potential of regenerative medicine in cutaneous wound healing. INT WOUND J 2017;14:450-459.
6. Ijaola AO, Akamo DO, Damiri F, Akisin CJ, Bamidele EA, Ajiboye EG, Berrada M, Onyenokwe VO, Yang SY, Asmatulu E: Polymeric biomaterials for wound healing applications: A comprehensive review. J Biomater Sci Polym Ed 2022:1-53.
7. Mir M, Ali MN, Barakullah A, Gulzar A, Arshad M, Fatima S, Asad M: Synthetic polymeric biomaterials for wound healing: A review. Prog Biomater 2018;7:1-21.
8. Ding J, Zhang J, Li J, Li D, Xiao C, Xiao H, Yang H, Zhuang X, Chen X: Electrospun polymer biomaterials. PROG POLYM SCI 2019;90:1-34.
9. Feng X, Li J, Zhang X, Liu T, Ding J, Chen X: Electrospun polymer micro/nanofibers as pharmaceutical repositories for healthcare. J CONTROL RELEASE 2019;302:19-41.
10. Hassanshahi A, Hassanshahi M, Khabbazi S, Hosseini-Khah Z, Peymanfar Y, Ghalamkari S, Su YW, Xian CJ: Adipose-derived stem cells for wound healing. J CELL PHYSIOL 2019;234:7903-7914.
11. Kim YJ, Jeon HR, Kim SW, Kim YH, Im GB, Im J, Um SH, Cho SM, Lee JR, Kim HY, Joung YK, Kim DI, Bhang SH: Lightwave-reinforced stem cells with enhanced wound healing efficacy. J TISSUE ENG 2021;12:1758557308.
12. Li R, Liu K, Huang X, Li D, Ding J, Liu B, Chen X: Bioactive materials promote wound healing through modulation of cell behaviors. ADV SCI 2022;9:2105152.
13. Han Y, Li X, Zhang Y, Han Y, Chang F, Ding J: Mesenchymal stem cells for regenerative medicine. CELLS-BASEL 2019;8:886.
14. Hu JC, Zheng CX, Sui BD, Liu WJ, Jin Y: Mesenchymal stem cell-derived exosomes: A novel and potential remedy for cutaneous wound healing and regeneration. WORLD J STEM CELLS 2022;14:318-329.
15. Zeitouni S, Krause U, Clough BH, Halderman H, Falster A, Blalock DT, Chaput CD, Sampson HW, Gregory CA: Human mesenchymal stem cell-derived matrices for enhanced osteoregeneration. SCI TRANSL MED 2012;4:132r-155r.
16. Carstens MH, Quintana FJ, Calderwood ST, Sevilla JP, Rios AB, Rivera CM, Calero DW, Zelaya ML, Garcia N, Bertram KA, Rigdon J, Dos-Anjos S, Correa D: Treatment of chronic diabetic foot ulcers with adipose-derived stromal vascular fraction cell injections: Safety and evidence of efficacy at 1 year. Stem Cells Transl Med 2021;10:1138-1147.

17. Groll J, Burdick JA, Cho D, Derby B, Gelinsky M, Heilshorn SC, Jüngst T, Malda J, Mironov VA, Nakayama K, Ovsianikov A, Sun W, Takeuchi S, Yoo JJ, Woodfield TBF: A definition of bioinks and their distinction from biomaterial inks. BIOFABRICATION 2018;11:13001.
18. Yang A, Huang Z, Yin G, Pu X: Fabrication of aligned, porous and conductive fibers and their effects on cell adhesion and guidance. Colloids Surf B Biointerfaces 2015;134:469-474.
19. Xie C, Gao Q, Wang P, Shao L, Yuan H, Fu J, Chen W, He Y: Structure-induced cell growth by 3D printing of heterogeneous scaffolds with ultrafine fibers. MATER DESIGN 2019;181:108092.
20. Gao D, Zhou JG: Designs and applications of electrohydrodynamic 3D printing. Int J Bioprint 2019;5:172.
21. Chang J, He J, Lei Q, Li D: Electrohydrodynamic printing of microscale PEDOT:PSS-PEO features with tunable Conductive/Thermal properties. ACS Appl Mater Interfaces 2018;10:19116-19122.
22. Taskin MB, Ahmad T, Wistlich L, Meinel L, Schmitz M, Rossi A, Groll J: Bioactive electrospun fibers: Fabrication strategies and a critical review of Surface-Sensitive characterization and quantification. CHEM REV 2021;121:11194-11237.
23. Dziadek M, Dziadek K, Checinska K, Zagrajczuk B, Golda-Cepa M, Brzychczy-Wloch M, Menaszek E, Kopec A, Cholewa-Kowalska K: PCL and PCL/bioactive glass biomaterials as carriers for biologically active polyphenolic compounds: Comprehensive physicochemical and biological evaluation. Bioact Mater 2021;6:1811-1826.
24. Li Y, Zhou J, Wu C, Yu Z, Zhang W, Li W, Zhang X: Development of cryogenic electrohydrodynamic jet printing for fabrication of fine scaffolds with extra filament surface topography. 3D PRINT ADDIT MANUF 2020;7:230-236.
25. Ravanbakhsh H, Luo Z, Zhang X, Maharjan S, Mirkarimi HS, Tang G, Chávez-Madero C, Mongeau L, Zhang YS: Freeform cell-laden cryobioprinting for shelf-ready tissue fabrication and storage. Matter 2022;5:573-593.
26. Li Z, Xu M, Wang J, Zhang F: Recent advances in cryogenic 3D printing technologies. ADV ENG MATER 2022;n/a:2200245.
27. Zhang Y, Ullah I, Zhang W, Ou H, Domingos M, Gloria A, Zhou J, Li W, Zhang X: Preparation of electrospun nanofibrous polycaprolactone scaffolds using nontoxic ethylene carbonate and glacial acetic acid solvent system. J APPL POLYM SCI 2020;137:48387.
28. Li W, Hu Y, Shi L, Zhang X, Xiong L, Zhang W, Ullah I: Electrospinning of Polycaprolactone/Pluronic F127 dissolved in glacial acetic acid: Fibrous scaffolds fabrication, characterization and in vitro evaluation. J Biomater Sci Polym Ed 2018;29:1155-1167.
29. Luo CJ, Stride E, Edirisinghe M: Mapping the influence of solubility and dielectric constant on electrospinning polycaprolactone solutions. MACROMOLECULES 2012;45:4669-4680.
30. Huang J, Liu Y, Chi X, Jiang Y, Xu Z, Qu G, Zhao Y, Li Z, Chen C, Chen G, Wu X, Ren J: Programming electronic skin with diverse skin-like properties. J MATER CHEM A 2021;9:963-973.
31. Sun Y, Chi X, Meng H, Ma M, Wang J, Feng Z, Quan Q, Liu G, Wang Y, Xie Y, Zheng Y, Peng J: Polylysine-decorated macroporous microcarriers laden with adipose-derived stem cells promote nerve regeneration in vivo. Bioactive Materials 2021;6:3987-3998.
32. Nussbaumer-Pröll AK, Eberl S, Reiter B, Stimpfl T, Jäger W, Poschner S, Zeitlinger M: Impact of thrombocytes, on bacterial growth and antimicrobial activity of selected antibiotics. EUR J CLIN MICROBIOL 2020;39:593-597.
33. Mayton HM, Walker SL, Berger BW: Disrupting irreversible bacterial adhesion and biofilm

22

formation with an engineered enzyme. Appl Environ Microbiol 2021;87:e26521.
34. Coffey BM, Anderson GG: Biofilm formation in the 96-well microtiter plate. Methods Mol Biol 2014;1149:631-641.
35. Norzain NA, Yu ZW, Lin WC, Su HH: Micropatterned fibrous scaffold produced by using Template-Assisted electrospinning technique for wound healing application. Polymers (Basel) 2021;13:2821.
36. Xue C, Sutrisno L, Li M, Zhu W, Fei Y, Liu C, Wang X, Cai K, Hu Y, Luo Z: Implantable multifunctional black phosphorus nanoformulation-deposited biodegradable scaffold for combinational photothermal/ chemotherapy and wound healing. BIOMATERIALS 2021;269:120623.
37. Huang J, Jiang Y, Liu Y, Ren Y, Xu Z, Li Z, Zhao Y, Wu X, Ren J: Marine-inspired molecular mimicry generates a drug-free, but immunogenic hydrogel adhesive protecting surgical anastomosis. Bioactive Materials 2021;6:770-782.
38. Mohania D, Chandel S, Kumar P, Verma V, Digvijay K, Tripathi D, Choudhury K, Mitten SK, Shah D: Ultraviolet radiations: Skin Defense-Damage mechanism. ADV EXP MED BIOL 2017;996:71-87.
39. Liu Y, Huang J, Xu Z, Li S, Jiang Y, Qu GW, Li Z, Zhao Y, Wu X, Ren J: Fabrication of gelatin-based printable inks with improved stiffness as well as antibacterial and UV-shielding properties. INT J BIOL MACROMOL 2021;186:396-404.
40. Derakhshanfar S, Mbeleck R, Xu K, Zhang X, Zhong W, Xing M: 3D bioprinting for biomedical devices and tissue engineering: A review of recent trends and advances. Bioact Mater 2018;3:144-156.
41. Sears NA, Seshadri DR, Dhavalikar PS, Cosgriff-Hernandez E: A review of Three-Dimensional printing in tissue engineering. Tissue Eng Part B Rev 2016;22:298-310.
42. Laronda MM, Rutz AL, Xiao S, Whelan KA, Duncan FE, Roth EW, Woodruff TK, Shah RN: A bioprosthetic ovary created using 3D printed microporous scaffolds restores ovarian function in sterilized mice. NAT COMMUN 2017;8:15261.
43. Sens P: Stick-slip model for actin-driven cell protrusions, cell polarization, and crawling. Proc Natl Acad Sci U S A 2020;117:24670-24678.
44. Barrientos S, Stojadinovic O, Golinko MS, Brem H, Tomic-Canic M: Growth factors and cytokines in wound healing. WOUND REPAIR REGEN 2008;16:585-601.
45. Yen JH, Chio WT, Chuang CJ, Yang HL, Huang ST: Improved wound healing by naringin associated with MMP and the VEGF pathway. MOLECULES 2022;27:1695.
46. Martin P, Nunan R: Cellular and molecular mechanisms of repair in acute and chronic wound healing. Br J Dermatol 2015;173:370-378.
47. Guan Y, Niu H, Liu Z, Dang Y, Shen J, Zayed M, Ma L, Guan J: Sustained oxygenation accelerates diabetic wound healing by promoting epithelialization and angiogenesis and decreasing inflammation. SCI ADV 2021;7: eabj0153.
48. Hwang NS, Zhang C, Hwang YS, Varghese S. Mesenchymal stem cell differentiation and roles in regenerative medicine. Wiley Interdiscip Rev Syst Biol Med. 2009, 1:97-106.

23

Figures and Figure legends

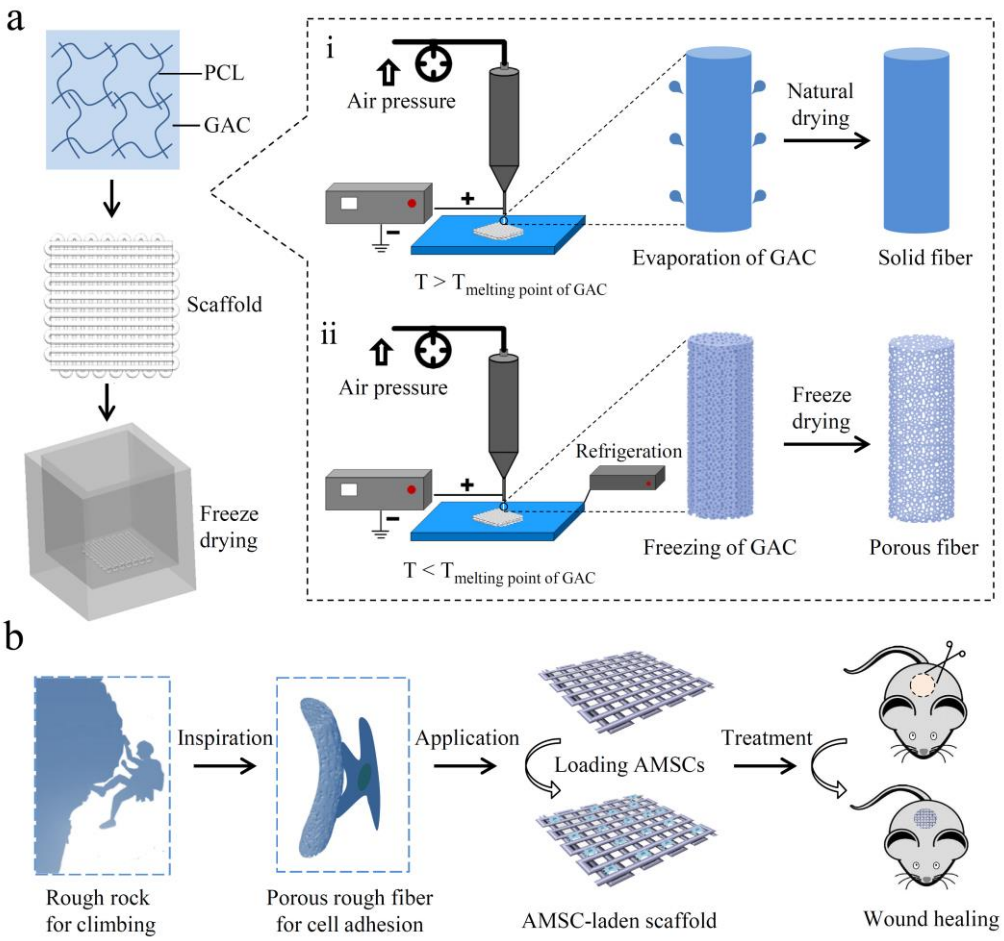

Fig. 1. Schematic diagram of rock climbing-inspired EHD cryoprinted porous fiber scaffolds with enhanced MSC therapeutic potential for wound healing. (a) The principle description of the porous structure formed by EHD cryoprinting based on the restoration of GAC in the fibers. i, without cryoprinting; ii, with cryoprinting. (b) Increased AMSC adhesion to scaffolds based on biomaterial topography inspired by rock climbing was expected to improve wound healing.

24

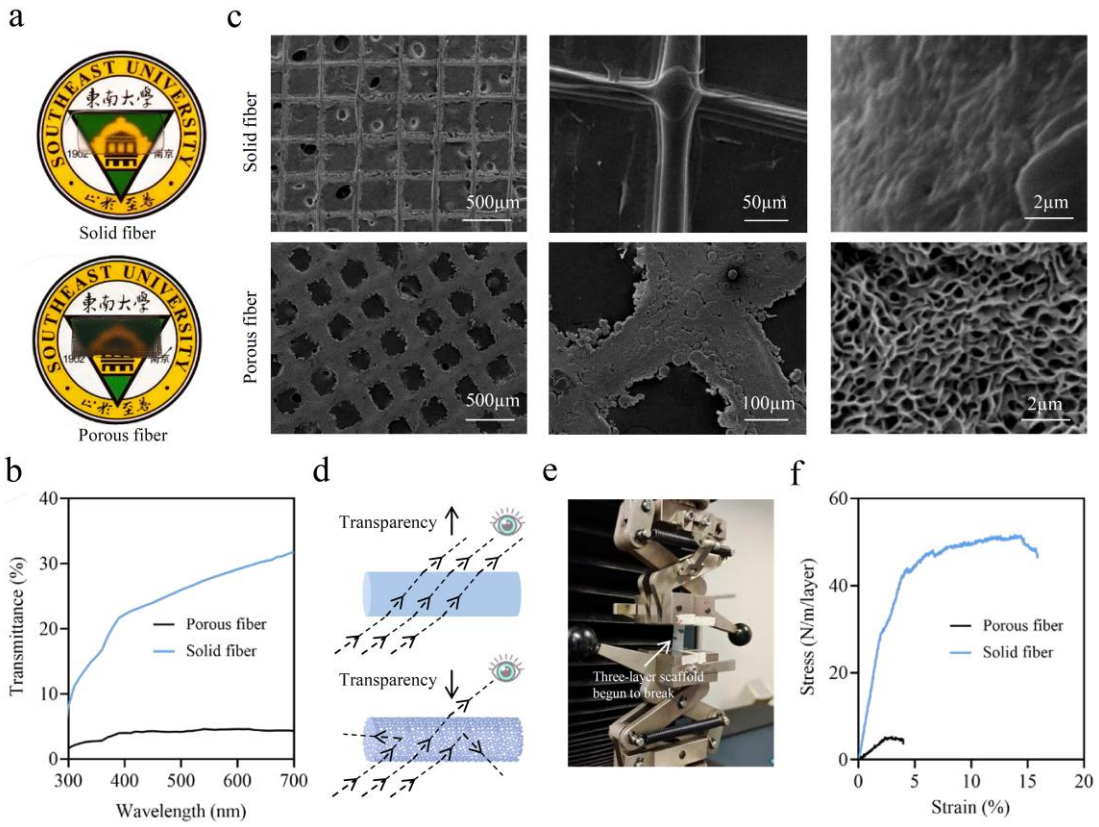

Fig. 2. Physical property changes generated by EHD cryoprinting for PCL scaffolds. (a) The university logo became less transparent when covered with the scaffold generated by cryoprinting. (b) Quantitative measurement of the transmittance of PCL scaffolds with or without cryoprinting. (c) The presence of a specific porous structure in the fibers of PCL scaffolds fabricated with cryoprinting. (d) Illustration explaining the reasons for the reduction in the transparency of scaffolds due to the pore-induced increase in light scattering. (e) The image recording the torn porous fiber scaffold after stretching. (f) The tensile stress−strain curve of three-layer scaffolds with a porous structure or solid structure.

25

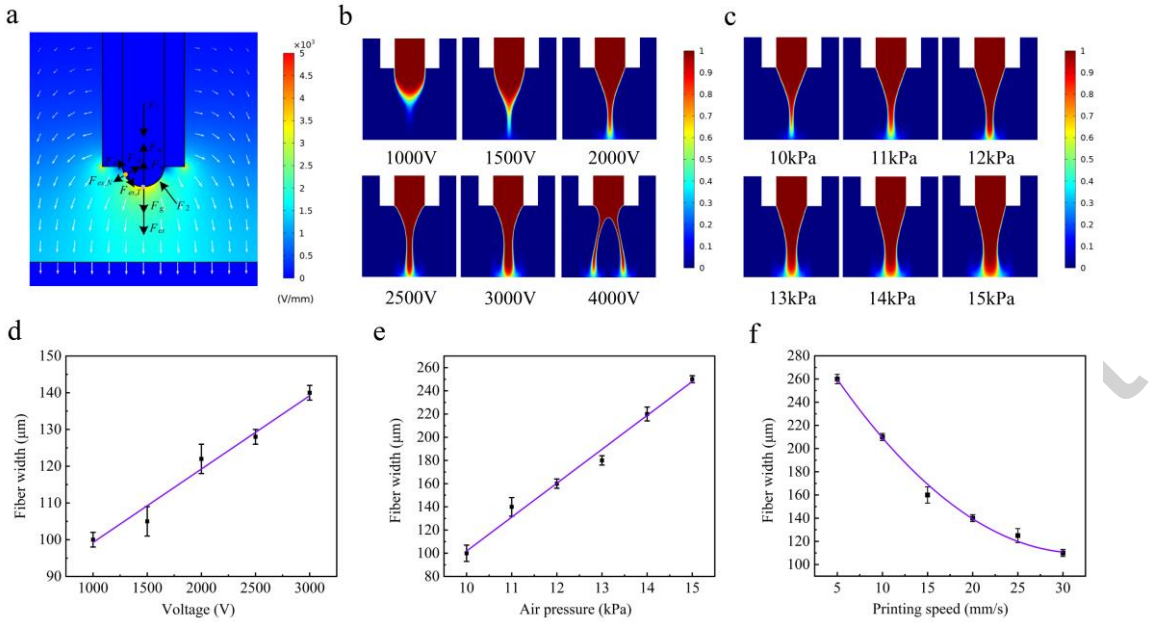

Fig. 3. Size modulation of cryoprinted fibers based on the voltage, pressure of the air pump, and printing speed. (a) Force analysis of a Taylor cone during EHD printing in a coupled flow and electric field. The gray dot represents the lowest position of the Taylor cone with an unequal force action to allow the liquid to be expelled downward. The yellow dot was located at the lateral part of the Taylor cone, and the force in the N direction was balanced to ensure that the conical jet was stable. (b) Simulation of a conical jet using different voltages. (c) Simulation of the conical jet under different pressures provided by the air pump. (d) The actual fiber width fabricated with different voltages, n = 3. (e) The actual fiber width was regulated by different air pressures, n = 3. (f) The actual fiber width manufactured with different printing speeds, n = 3.

26

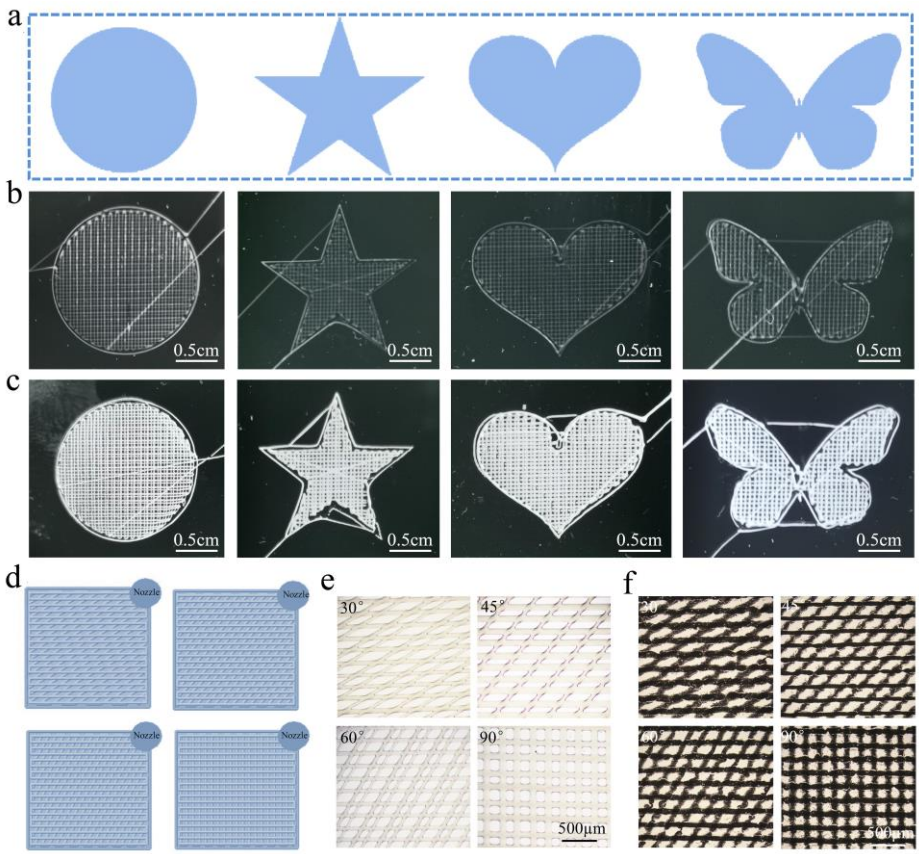

Fig. 4. The customized shapes and micropatterns of PCL scaffolds. (a) The different shapes designed for printing. (b) Actual EHD printed solid fiber scaffolds in different shapes. (c) Actual EHD cryoprinted porous fiber scaffolds in different shapes. (d) The different printing paths with the fibers crossed at 30°, 45°, 60°, or 90° designed for the micropatterned scaffolds. (e) Actual EHD printed solid fiber scaffolds with the fibers crossed at different angles. (f) Actual EHD cryoprinted porous fiber scaffolds with the fibers crossed at different angles.

27

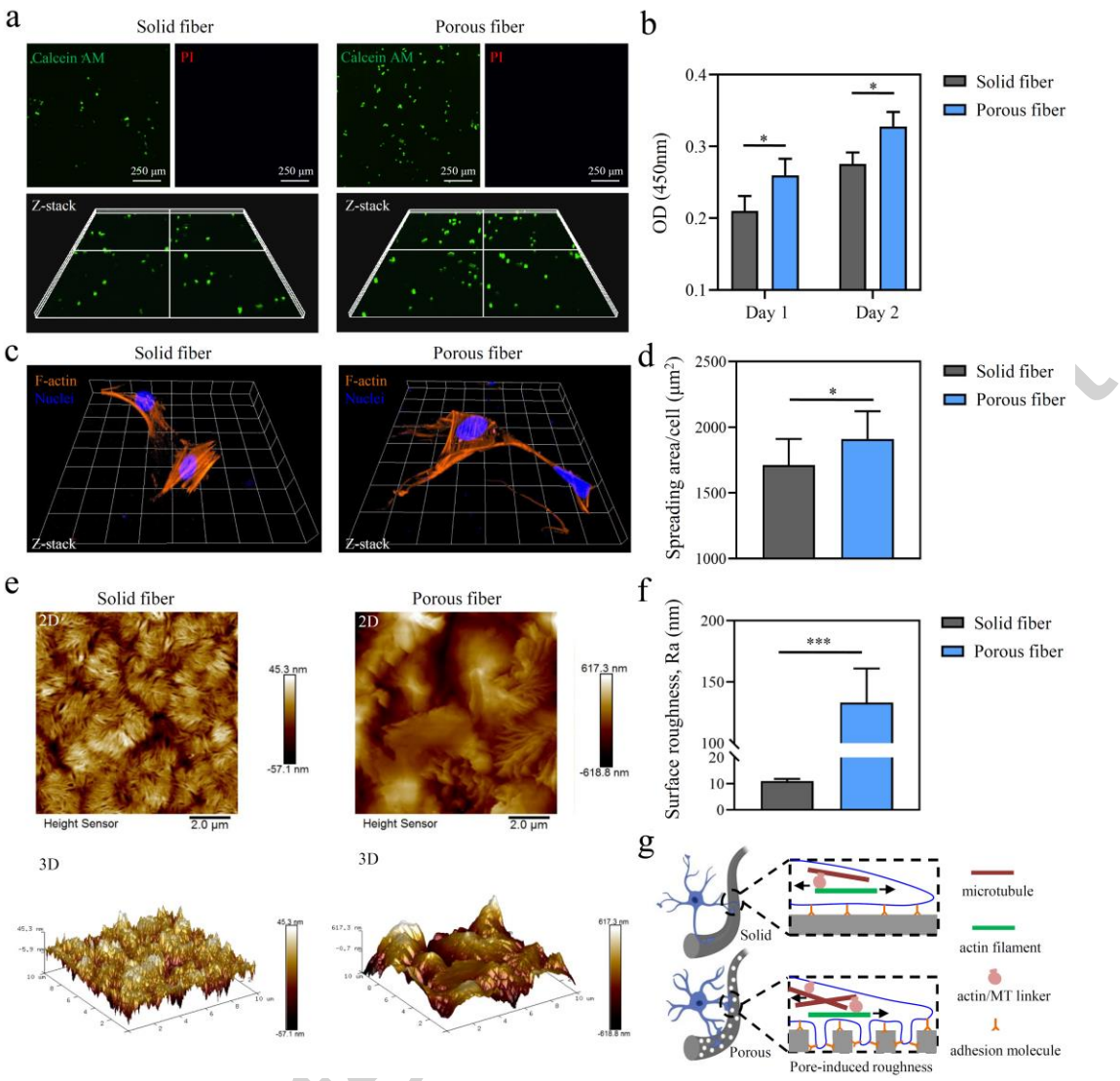

Fig. 5. Improved AMSC adhesion to EHD cryoprinted PCL scaffolds was due to surface roughening. (a) Live/dead staining of AMSCs adhered to the solid fiber scaffold or porous fiber scaffold after eight hours of co-culture. (b) CCK-8 analysis of the cell counts of AMSCs attached to different scaffolds on Day 1 and Day 2, n = 3. (c) Z-Stack images of the cytoskeleton F-actin of AMSCs attached to different scaffolds after eight hours of co-culture. (d) The average cell spreading surface when cultured on the solid fiber scaffold or porous fiber scaffold, n=15. (e) 2D and 3D images of fiber surfaces detected with AFM. (f) Ra calculated from the mean surface roughness of fibers, n = 5. (g) A schematic diagram demonstrating that cryoprinting-mediated porous structure formation enlarging the surface roughness of scaffolds improved AMSC adhesive abilities by providing more binding sites for adhesion molecules. MT, microtubule. *, $P < 0.05$; ***, $P < 0.001$.

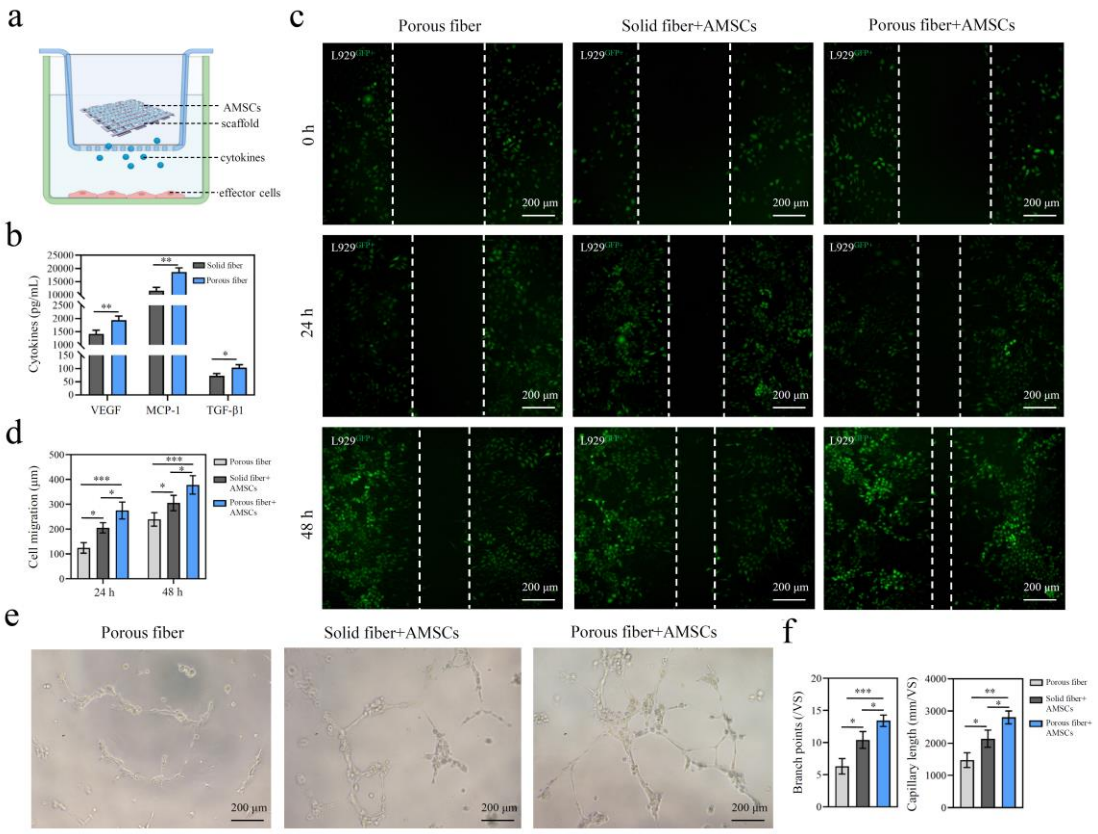

Fig. 6. The increase in AMSC adhesion improved cell therapy *in vitro* due to the enhanced paracrine action. (a) The transwell model constructed to evaluate the functions of AMSC-laden scaffolds on different effector cells. (b) The cytokines VEGF, MCP-1, and TGF-β1 secreted from AMSCs adhering to different scaffolds, n = 3. (c) The effects on wound healing of fibroblasts treated with AMSCs adhering to different scaffolds. (d) Quantitative analysis of the fibroblast migration speed, n = 3. (e) The effects HUVECs treated with AMSCs adhering to different scaffolds on tube formation. (f) Quantitative analysis of the branched points and capillary length of HUVECs, n = 3. *, $P < 0.05$; **, $P < 0.01$; ***, $P < 0.001$.

29

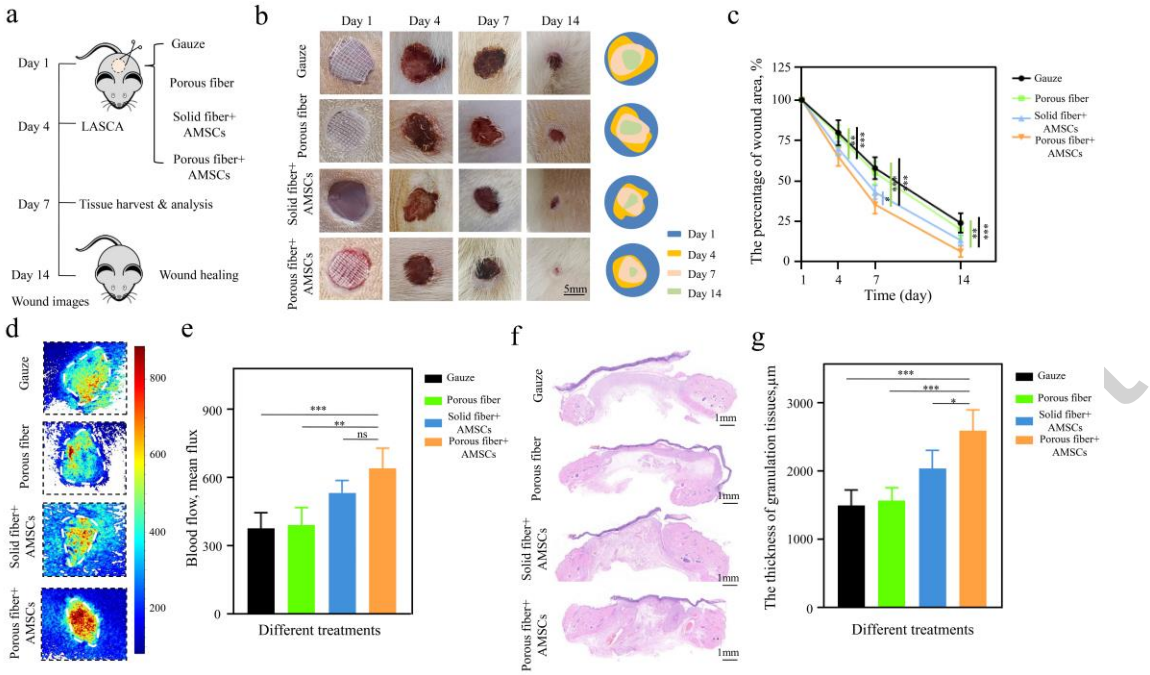

Fig. 7. The AMSC-laden porous fiber scaffolds improved cell therapy for wound healing *in vivo*. (a) The animal intervention protocols. (b) Images recording the wound healing process after different treatments. (c) Quantitative analysis of the wound healing area after different treatments. (d) The evaluation of blood flow supply for wound repair on the 4th day postoperatively with LASCA using moorFLPI-2. (e) Quantitative analysis of blood flow supply based on the calculated mean flux, n = 4. (f) Representative HE staining images of regenerated granulation tissues in the defective wounds with different treatments. (g) Measurement of the granulation tissue thickness, n = 4. *, P < 0.05; **, P < 0.01; ***, P < 0.001; ns, not significant.

30

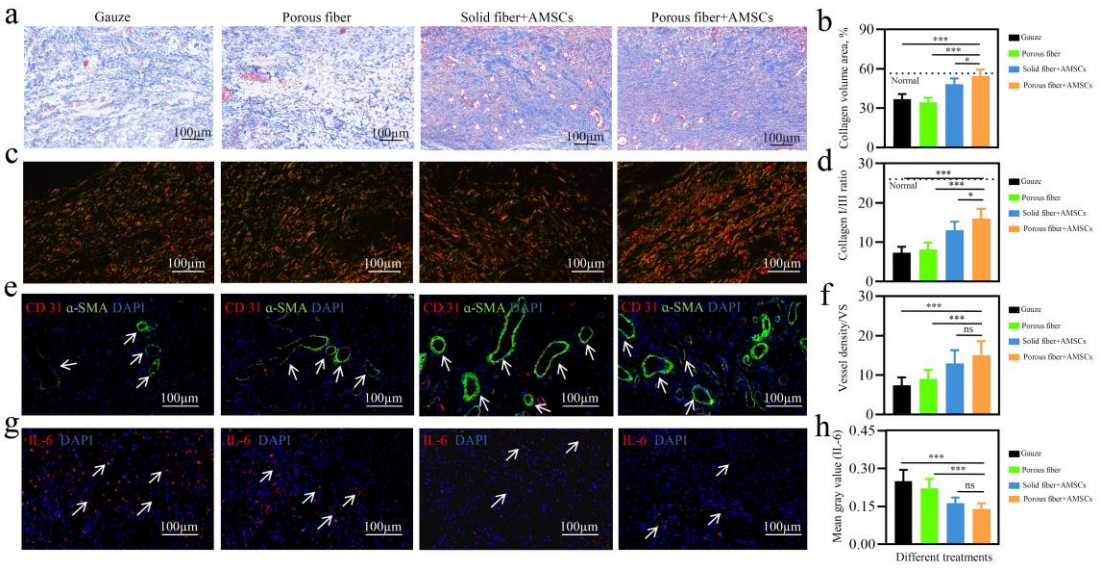

Fig. 8. Histological analysis of regenerated tissues after different treatments. (a) Masson's trichrome staining. (b) Quantitative analysis of the collage volume area, n = 8. (c) Sirius red staining. (d) Quantitative analysis of the collagen I/III ratio, n = 8. (e) IF staining of vascular structures with CD31 antibody and α-SMA. (f) Quantitative analysis of vessel density, n = 8. VS, visual field. (g) IF staining of the proinflammatory cytokine IL-6. (h) Quantitative analysis of IL-6 expression, n = 8. *, $P < 0.05$; ***, $P < 0.001$; ns, not significant.

31